Journal of Alloys and Compounds 480 (2009) 521–528

Contents lists available at ScienceDirect

Journal of Alloys and Compounds

journal homepage: www.elsevier.com/locate/jallcom

# Structural and electrochemical properties of $Ti_xZr_{7-x}Ni_{10}$

K. Young[a,*], T. Ouchi[a], Y. Liu[b], B. Reichman[a], W. Mays[a], M.A. Fetcenko[a]

[a] Energy Conversion Devices Inc./Ovonic Battery Company, 2983 Waterview Drive, Rochester Hills, MI 48309, USA
[b] Department of Chemistry, Wayne State University, 5101 Cass Avenue, Detroit, MI 48202, USA

ARTICLE INFO

*Article history:*
Received 17 December 2008
Received in revised form 20 January 2009
Accepted 22 January 2009
Available online 6 February 2009

*Keywords:*
Hydrogen absorbing materials
Transition metal alloys and compounds
Metal hydride
Electrochemical reactions

ABSTRACT

Simple ternary alloys with formula $Ti_xZr_{7-x}Ni_{10}$ ($x$ between 0 and 2.5) were studied as a potential replacement for Laves phase alloys used in the negative electrodes of nickel metal hydride batteries. The samples were prepared by arc-melting and were not annealed. The samples retained a high degree of disorder, which contributed positively to activation and other electrochemical properties. Before hydrogenation, the alloys have a $Zr_7Ni_{10}$ orthorhombic structure mixed with some C15 and $ZrO_2$ secondary phases. The amount of C15 secondary phase is important to the bulk diffusion of hydrogen and the surface electrochemical kinetics. That is, the diffusion coefficient and the exchange current both increase in the presence of C15 secondary phase. The proportion of C15 secondary phase is controllable by stoichiometry design. For instance, a slightly higher Zr content reduces the C15 content. Further, as the titanium substitution level increases: (1) the lattice constants decrease; (2) the PCT plateau pressure increases; (3) activation becomes easier; and (4) the high rate dischargeability improves.



## 1. Introduction

Orthorhombic $Zr_7Ni_{10}$ (space group *Cmca* [1]) is an important secondary phase found in multi-component Laves phase based alloys used in nickel-metal hydride (NiMH) batteries [2–11]. The synergistic effect between the Zr–Ni phase and the Laves phase has been studied by a number of different groups [5,12–17]. Although it has a considerable amount of hydrogen storage capacity (H/M of about 0.9 at 60 °C [18,19]), the absorption/desorption kinetics of $Zr_7Ni_{10}$ is slow and not suitable for the main working phase in the negative electrode of batteries [12,13,15]. It has been shown by other groups that charging $Zr_7Ni_{10}$ chemically with hydrazine will produce a material having an electrochemical capacity of 268 mAh/g [20]. Badding et al. proposed a pulse charging method to improve the discharge capacity of $Zr_7Ni_{10}$, at a rate of 33 mA/g, from 50 to 142 mAh/g [21].

The electrochemical properties of $Ti_{1-x}Zr_xNi_{1+0.43x}$ containing $Zr_7Ni_{10}$ phase have been studied [22]. The partial substitution of Ti did not change the maximum discharge capacity significantly but improved the activation, with a concurrent trade-off in cycle life. Partial replacement of Ni by Cu in $Zr_7Ni_{10}$ did not change the orthorhombic structure [23]. The maximum solubility of copper in $Zr_7Ni_{10}$ was found to be around 7% [24]. In the case of partial replacement of Zr by Hf, the orthorhombic structure remains the same for the entire composition ranging from $Zr_7Ni_{10}$ to $Hf_7Ni_{10}$ [25]. Over-stoichiometric $(Ti_xZr_{1-x})_7(M_yNi_{1-y})_{10+z}$ alloys, where M is at least one element from V, Al, Cr, Co, Mn, Fe, and Cu, prepared by zone solidification and refining have been studied [26]. A long cycle life $(Ti_{0.4}Zr_{0.6})_7(Ni_{0.6}Mn_{0.1}Co_{0.1}V_{0.1})_{11.2}$ alloy achieved discharge capacities of 235, 330, 320, and 307 mAh/g after 1st, 25th, 100th, and 500th cycles, respectively, at a rate of 70 mA/g.

The present study investigates the potential use of $Zr_7Ni_{10}$ based alloy in the negative electrodes of NiMH batteries. The metal-hydrogen bond strength in the hydride of $Zr_7Ni_{10}$ is too strong to be used in battery application as seen from its relatively low heat of hydride formation (−47 kJ/mol $H_2$ [19]). Therefore the first task is to reduce the strength of metal hydrogen bond strength by partially replacing zirconium atoms with smaller titanium atoms as was previously done just with C14 based Zr–Ni alloys [27]. The second task is to increase the degree of disorder to improve the strong rate-dependence in the discharge capacity and ease of activation of base $Zr_7Ni_{10}$ alloy either by increasing the number of secondary phases or more synergetic interaction between phases with the additional modifier [28]. The addition of titanium to accomplish both objectives will be discussed in detail. This paper also lays the foundation for further studies in the $Zr_7Ni_{10}$ alloy family with additional modifiers reaching 357 mAh/g [29].

## 2. Experimental setup

Arc melting was performed under a continuous argon flow with a non-consumable tungsten electrode and a water-cooled copper tray. Before each arc melt, a piece of sacrificial titanium underwent a melting-cooling cycle a few times to reduce the residual oxygen concentration. Each 5 g ingot was re-melted and turned over a few times to ensure uniformity in the chemical composition. The chemical composition of each sample was examined by a Varian *Liberty* 100 inductively

* Corresponding author. Tel.: +1 248 293 7000; fax: +1 248 299 4520.
*E-mail address:* kwoyoung@yahoo.com (K. Young).

0925-8388/$ – see front matter © 2009 Elsevier B.V. All rights reserved.
doi:10.1016/j.jallcom.2009.01.117

**Table 1**
Structural and electrochemical properties of $Ti_xZr_{7-x}Ni_{10}$ alloys.

| Alloy name | Formula | XRD phases | | | | | ΔH in kJ/mol | ΔS in J/K mol | Maximum H-storage at 60 °C | Maximum capacity (mAh/g) | High rate dischargeability | Diffusion coefficient, D ($\times 10^{-10}$ cm$^2$/s) | Exchange current density, $I_o$ (mA/g) |
|---|---|---|---|---|---|---|---|---|---|---|---|---|---|
| | | Before PCT | After PCT | a (Å) | b (Å) | c (Å) | | | | | | | |
| ZN01 | $Zr_7Ni_{10}$ | O+C15 | T+C15 | 9.124 | 9.186 | 12.344 | −50 | −144 | 1.41% | 205 | 54% | 5.7 | 16.0 |
| ZN02 | $Ti_{0.5}Zr_{6.5}Ni_{10}$ | O+C15 | T+C15 | 9.090 | 9.151 | 12.298 | −33 | −115 | 1.27% | 188 | 46% | 10.2 | 15.5 |
| ZN03 | $Ti_{1.0}Zr_{6.0}Ni_{10}$ | O+C15 | O+T+C15 | 9.058 | 9.119 | 12.255 | −37 | −108 | 1.15% | 189 | 74% | 12.5 | 15.2 |
| ZN04 | $Ti_{1.5}Zr_{5.5}Ni_{10}$ | O | T | 9.028 | 9.089 | 12.214 | −37 | −101 | 1.20% | 204 | 79% | 9.6 | 8.4 |
| ZN05 | $Ti_{2.0}Zr_{5.0}Ni_{10}$ | O | T | 8.994 | 9.055 | 12.168 | – | – | 1.19% | 205 | 84% | 13.7 | 12.0 |
| ZN06 | $Ti_{2.5}Zr_{4.5}Ni_{10}$ | O+C15 | T | 8.963 | 9.023 | 12.126 | – | – | 1.11% | 190 | 81% | 12.1 | 21.9 |

O and T denote orthorhombic and tetragonal structures, respectively. Lattice constants are from orthorhombic structure before PCT measurements.




**Fig. 1.** XRD spectra using Cu Kα as the radiation source for as-prepared alloys ZN01 (a), ZN02 (b), ZN03 (c), ZN04 (d), ZN05 (e), ZN06 (f). White arrows indicate peaks only exist in the orthorhombic and not the tetragonal structure. Black arrows indicate peaks from C15 secondary phase.

coupled plasma (ICP) system. A Philips *X'Pert Pro* X-ray Diffractometer (XRD) was used to study each alloy's microstructure. A JOEL-*JSM6320F* Scanning Electron Microscope (SEM) with Energy Dispersive Spectroscopy (EDS) capability, a Hitachi S-2400 SEM with EDS, backscattering electron (BSE), and electron backscattering diffraction (EBSD) capabilities were used to study the microstructure and composition. PCT characteristics for each sample were measured using a Suzuki-Shokan multi-channel PCT system. In the PCT analysis, each sample was first activated by a 2 h thermal cycle between 300 °C and room temperature at 25 atm $H_2$ pressure. Electrochem-




**Fig. 2.** XRD spectra using Cu Kα as the radiation source for after PCT alloys ZN01 (a), ZN02 (b), ZN03 (c), ZN04 (d), ZN05 (e), ZN06 (f). White arrows indicate peaks only exist in the orthorhombic structure. Black arrows indicate peaks from C15 secondary phase.

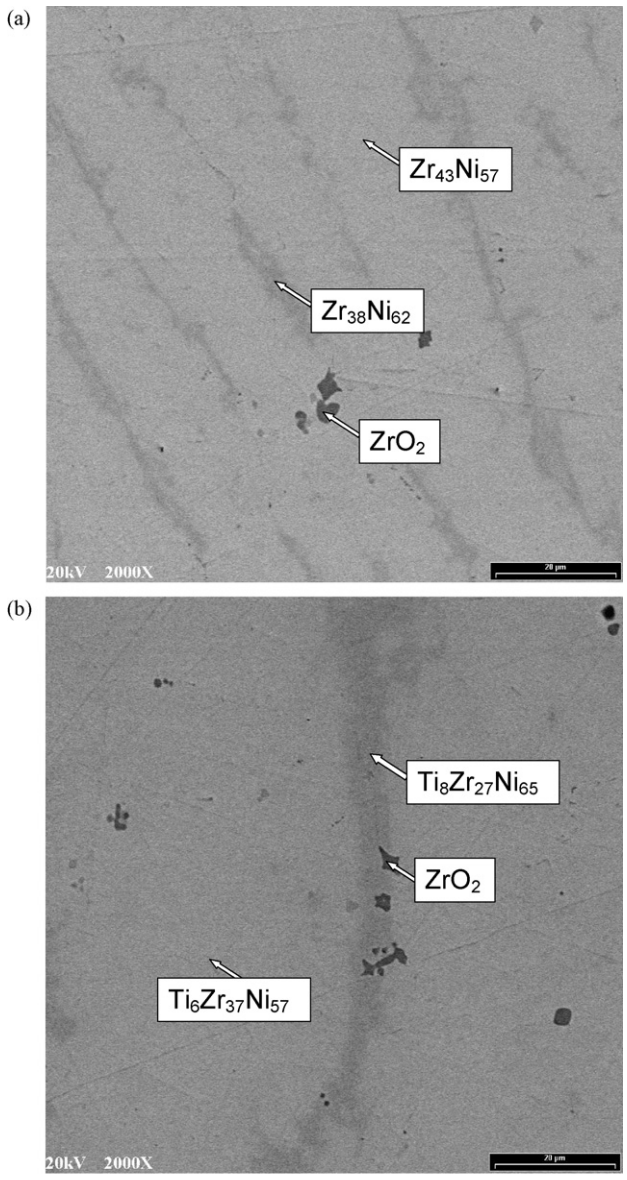


**Fig. 3.** SEM backscattering electron image micrographs for alloys ZN01 (a) and ZN03 (b). The bar on the right lower corner indicates a length of 20 μm. Compositions identified in the micrograph are from EDS analysis.

ical measurements were performed with a Solartron 1470 cell test multi-channel potentiostat and a Solartron 1250 Frequency Response Analyzer.

For discharge capacity and electrochemical study, the ingot was first ground and then passed through a 200 size mesh sieve. The sieved powder was then compacted onto an expanded nickel metal substrate by a 10 ton press to form a test electrode (about 1 $cm^2$ in area and 0.2 mm thick) without using any binder. Discharge capacities of these small sized electrodes were measured in a flooded cell configuration using a partially pre-charged $Ni(OH)_2$ pasted electrode as the positive electrode and a 6 M KOH solution as the electrolyte. The system was charged at a current density of 50 mA/g for 6 h and then discharged at a current density of 50 mA/g until a cut-off voltage of −0.9 V was reached. The system was then discharged at a current density of 12 mA/g until a cut-off voltage of −0.9 V was reached and finally discharged at a current density of 4 mA/g until a cut-off voltage of −0.9 V was reached. Linear polarization was performed by scanning the potential from −20 to +20 mV of the open circuit voltage at a rate of 0.1 mV/s. For the potentiostatic discharge experiments electrodes in a fully charged state were polarized +0.6 V vs. the open circuit voltage for 5400 s.

## 3. Results and discussion

Six alloys, ZN01 to ZN06, were prepared by arc melting with no subsequent annealing treatment. Target compositions of these

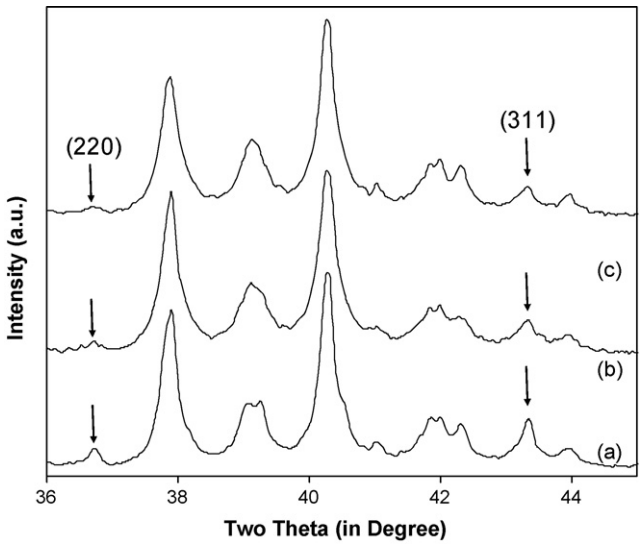


**Fig. 4.** XRD spectra using Cu Kα as the radiation source for as-prepared alloys ZN01 (a), ZN01 formula with additional 1 wt% Zr (b), and ZN01 formula with additional 2 wt% Zr (c). Black arrows indicate peaks from C15 secondary phase.

alloys are listed in Table 1. The final chemical composition of each sample was verified by ICP to be within 0.1 wt% from designed values. Although the literature suggested the use of a long annealing period to purify the $Zr_7Ni_{10}$ phase (1000 °C for 1 day [1], 3 days [30] or one month [12,15]), we omitted the annealing step due to the practicability in mass production and the potential synergistic advantages from minor phases [10,13,15]. An example of this is the multi-phase Laves-$ZrNi_x$ alloys, in which the amount of secondary phase decreases during annealing treatment, thereby causing the general electrochemical properties to deteriorate due to lack of synergetic effects from the minor phases [14]. Maximum hydrogen storage capacity in $Zr_7Ni_{10}$ was not sacrificed with the elimination of the annealing step as can be seen in the comparison between the annealed sample [12] and the present work (1.36 vs. 1.38 wt% at 80 °C and 1.40 vs. 1.42 wt% at 25 °C, respectively).

### 3.1. Microstructure

There are two crystal structures reported for pure $Zr_7Ni_{10}$, orthorhombic (*Aba2* [31] or *Cmca* [32] space group) and tetragonal [1,30]. The later structure is only observed after hydriding/dehydriding. The orthorhombic XRD reflection peaks having one even and one odd *h* and *k* indicia (e.g. (2 1 1), (2 1 3), and (1 0 5)), disappear in the tetragonal spectrum due to a higher degree of symmetry [30] and such disappearance can be used to identify the existence of the tetragonal phase.

XRD analysis was performed on six as-prepared samples and the results are plotted in Fig. 1. Alloy ZN01 ($Zr_7Ni_{10}$) has a dominating orthorhombic structure as reported by Joubert et al. [16] with a secondary phase identified as a Laves C15 face-center-cubic structure. The white arrows in Fig. 1 point to peaks that only exist in orthorhombic and not the tetragonal structure. As the titanium substitution in the alloy increases, those orthorhombic-only peaks become less defined. The changes in peak shape can be attributed to either the co-existence of orthorhombic and tetragonal structures or changes in scattering factors with the addition of titanium atoms. Lattice constants of the main $Zr_7Ni_{10}$ phase were calculated from peak positions and listed in Table 1. As the amount of the titanium substitution in alloys increases, all three lattice parameters decrease monotonically due to the smaller atomic radius of titanium atom vs. that of the original zirconium atom (1.614 vs. 1.771 Å, values are from [33] in the Laves phase alloy). This reduction in cell

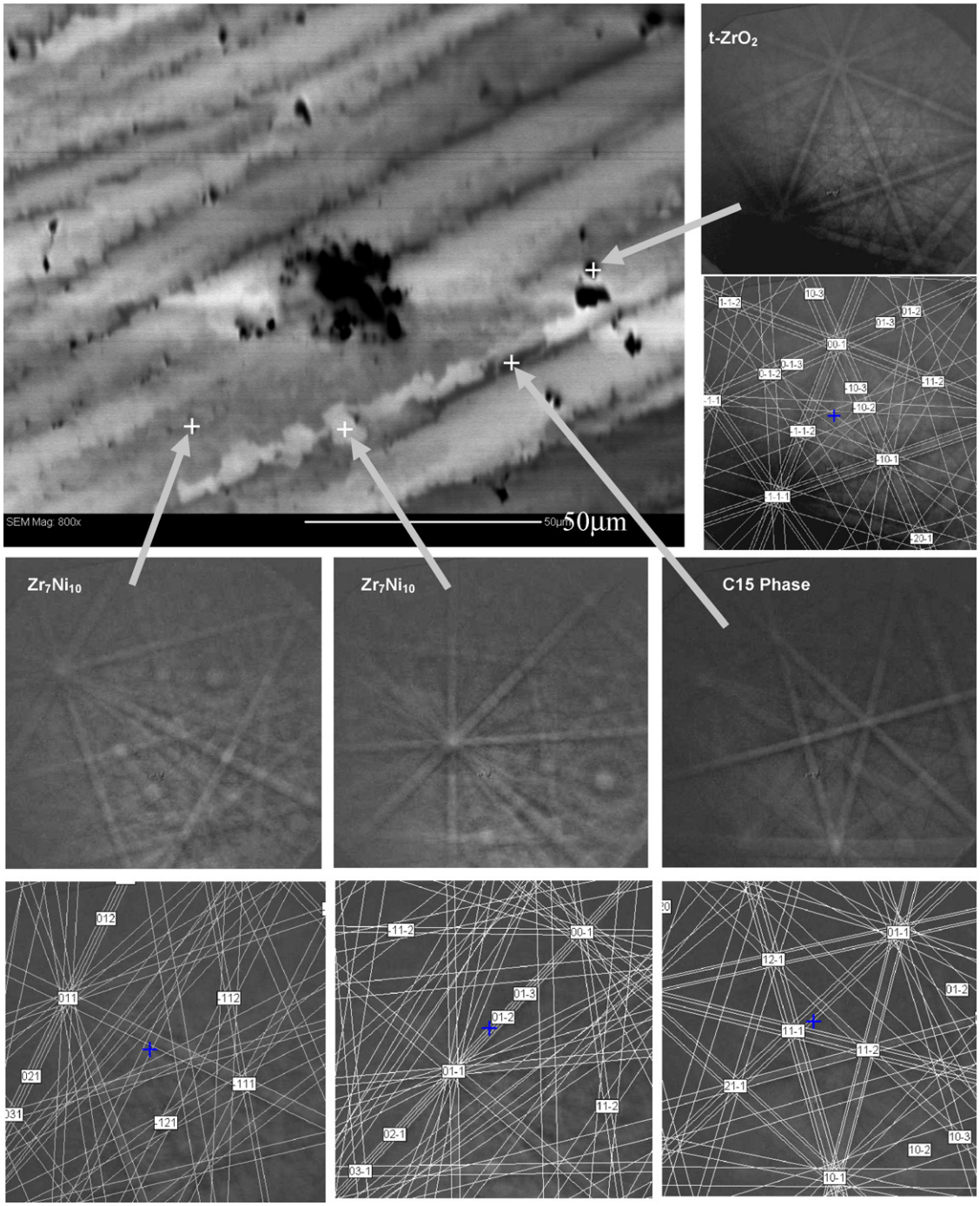


**Fig. 5.** SEM micrograph from a virgin ZN06 sample together with backscattering patterns and their computer simulation for two areas with an orthorhombic $Zr_7Ni_{10}$ structure, C15 phase at the boundary and a tetragonal $ZrO_2$ phase.

volume is consistent with the assumption that titanium atoms substitute for zirconium. A similar reduction in cell parameters was reported for substitution of smaller Hf atoms in $Hf_xZr_{7-x}Ni_{10}$ [1]. The amount of C15 secondary phase was undetectable by XRD for alloys ZN04 and ZN05.

XRD analysis was preformed again after PCT measurements and the results are plotted in Fig. 2. Samples were dehydrided down to the lowest pressure at 30 °C except for ZN01 which was dehydrided at 120 °C. The C15 minority phase did not change position, which indicates it has a higher plateau pressure (weaker metal-

**Table 2**
Chemical compositions in atomic percentage determined by EDS and the average electron concentration ($e/a$) of C15 secondary phase for alloys in this study.

| | ZN01 | ZN02 | ZN03 | ZN04 | ZN05 | ZN06 |
|---|---|---|---|---|---|---|
| Main phase | $Zr_{43}Ni_{57}$ | $Ti_2Zr_{40}Ni_{58}$ | $Ti_6Zr_{37}Ni_{57}$ | $Ti_8Zr_{35}Ni_{57}$ | $Ti_{13}Zr_{30}Ni_{57}$ | $Ti_{15}Zr_{28}Ni_{57}$ |
| C15 phase | $Zr_{38}Ni_{62}$ | $Ti_3Zr_{30}Ni_{67}$ | $Ti_8Zr_{27}Ni_{65}$ | $Ti_{11}Zr_{24}Ni_{65}$ | $Ti_6Zr_{19}Ni_{65}$ | $Ti_7Zr_{20}Ni_{63}$ |
| $e/a$ of C15 | 7.72 | 8.02 | 7.90 | 7.90 | 7.90 | 7.78 |

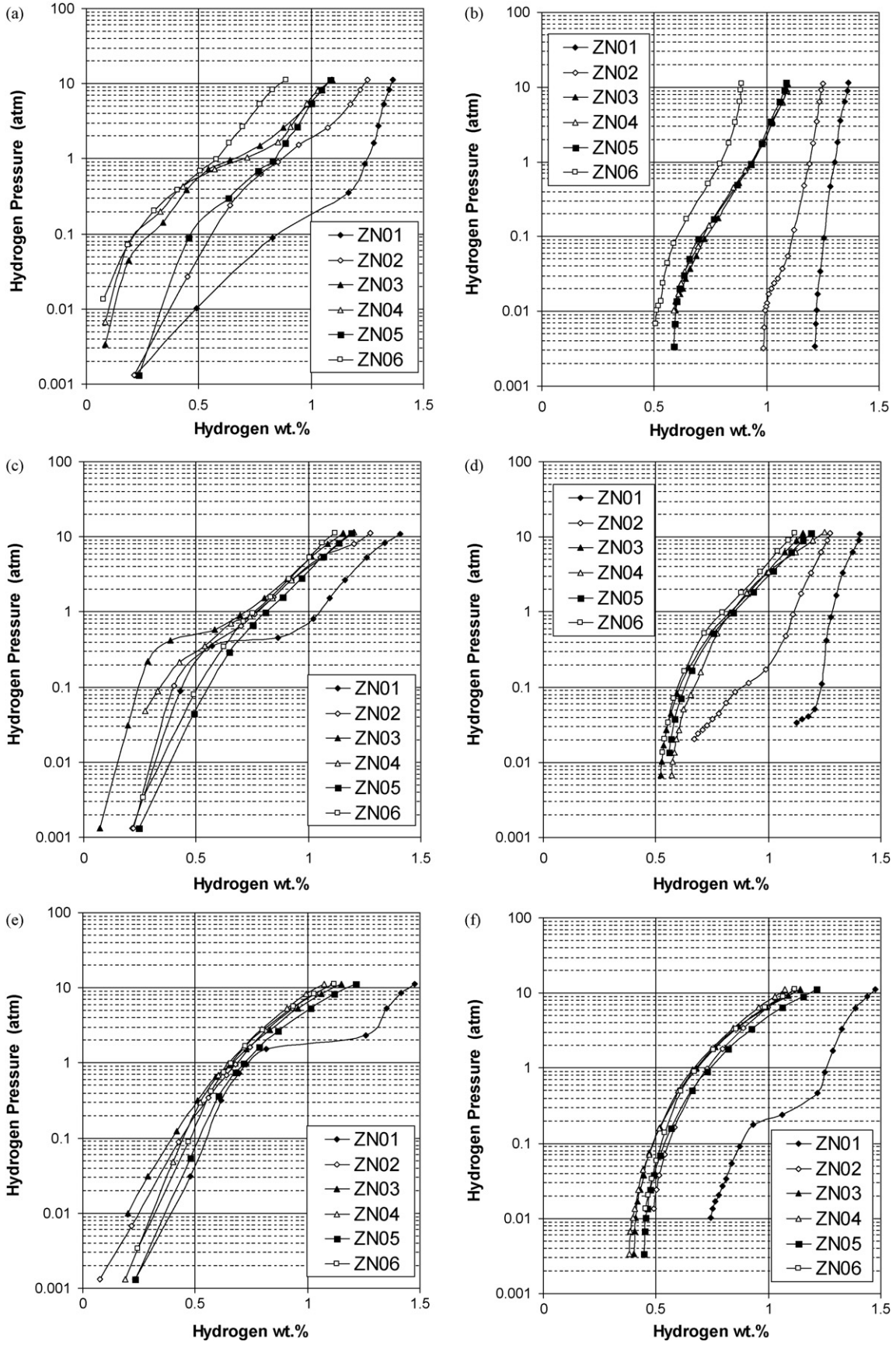


**Fig. 6.** PCT isotherms of alloys from ZN01 to ZN06 absorption at 30 °C (a), desorption at 30 °C (b), absorption at 60 °C (c), desorption at 60 °C (d), absorption at 90 °C (e), and desorption at 90 °C (f).

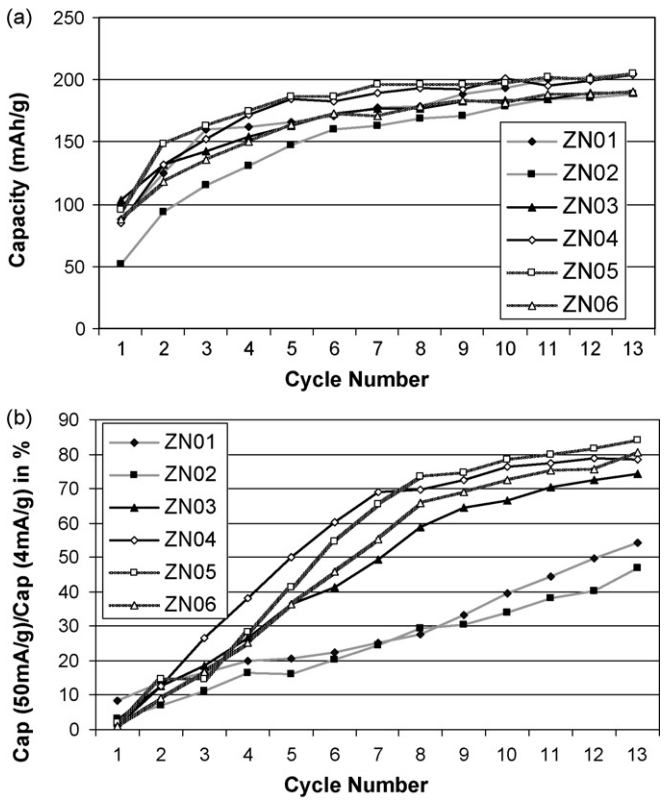


**Fig. 7.** Evolution of full discharge capacity at a rate of 4 mA/g (a) and ratio of capacities between 50 and 4 mA/g rates (b) as a function of cycle number for alloys ZN01 to ZN06.

hydrogen bond strength) than the main working $Zr_7Ni_{10}$ phase. The orthorhombic-only peaks disappeared in sample ZN01, which confirmed the finding by Takeshita et al. about the new tetrahedral phase [1]. Most of the Ti-substituted alloys (except ZN03) showed a complete switch from an orthorhombic structure into a tetragonal structure. The shift of XRD peaks into higher angles with higher titanium substitution indicates not only the unit cell becomes smaller but also the metal-hydrogen bond is weaker (more complete dehydride) in the case of a higher titanium content. The amount of C15 secondary phase remains undetectable by XRD technical for alloys ZN04, ZN05, and ZN06.

Backscattering electron micrographs from SEM analysis of ZN01 and ZN03 are shown in Fig. 3a,b, respectively, as examples. Compositions determined by EDS analysis of the majority of the scanned area are very close to the target composition. Zr-poor secondary phases (close to AB2 stoichiometry) were formed together with the inclusion of $ZrO_2$. Therefore we suspect there is a connection between the formation of AB2 secondary and localized non-stoichiometry due to $ZrO_2$ formation from the oxygen impurity in the arc melt chamber. Two new samples with additional 1 and 2 wt% Zr to ZN01 composition were prepared by the same arc melting method. XRD spectra from these two samples were compared with the original ZN01 in Fig. 4. Arrows in the figure indicate (2 2 0) and (3 1 1) reflections from a C15 structure. It was found that as the Zr content increased, the amount of C15 secondary phase decreased. This verifies that the formation of C15 Zr-poor secondary phase is related to the local Zr-content. For the remainder of this study, we do not try to eliminate or reduce the formation of C15 secondary phase. We believe the main phase will gain a synergetic effect with a C15 secondary phase acting as a dehydride catalyst due to its relatively higher equilibrium plateau pressure. The effect of over-stoichiometric (less Zr) $Zr_7Ni_{10}$ was previously studied [26]. As the composition, prepared by conventional arc melt, varied from

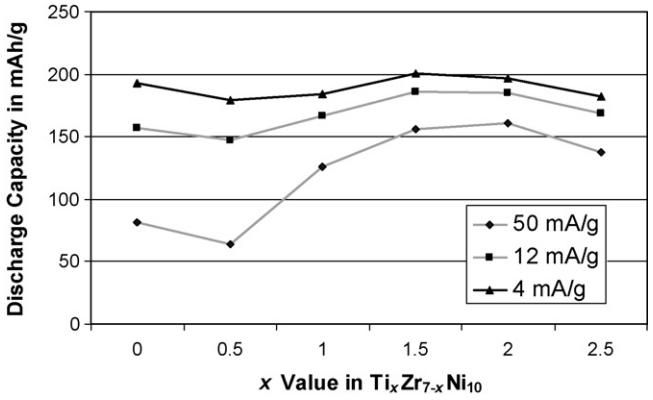


**Fig. 8.** Discharge capacities at cycle 10 with three rates as a function of $x$ in formula $Ti_xZr_{7-x}Ni_{10}$.

$Zr_7Ni_{10.1}$ to $Zr_7Ni_{10.6}$ and $Zr_7Ni_{11.2}$ the discharge capacity improved from 173, to 191 and 208 mAh/g [26]. This is a direct proof of synergetic effect between the main phase and the secondary phase as in the case of Laves phase-based alloy [10,15].

Next, SEM electron backscattering patterns were studied on a polished ZN06 sample in order to identify the source of smearing in the XRD orthorhombic only peak for the sample without the hydride–dehydride process and to verify the Laves phase structure at the grain boundary. A few representative channeling patterns with results from computer simulation are shown in Fig. 5. All areas with a $Zr_7Ni_{10}$ stoichiometry belong to the orthorhombic structure. No tetragonal $Zr_7Ni_{10}$ phase was found, which confirms that the smearing of the XRD peaks is caused by the change in scattering factor from the additional Ti The channeling pattern at the boundary confirms the existence of the C15 phase. The crystal structure of $ZrO_2$ in this case was found to be tetragonal which allows hydrogen to permeate and is beneficial for hydrogen diffusion in the alloy bulk.

The chemical compositions of AB2 secondary phase for each alloy are listed in Table 2. The numbers of shell electron per AB2 formula ranges from 26 to 27. This falls into the C15-dominant regime according to the tight binding calculation [34] and is consistent with our XRD analysis. Because the composition of Laves secondary phase plays an important role in the catalytic effect [35], the evolution of C15 secondary phase was examined. As the Ti-substitution increases, the Ti content in the C15 Laves phase increases in proportion to the Ti content in the main $Zr_7Ni_{10}$ phase initially and then drops to a lower level. The driving force for this drop in Ti content in C15 Laves phase is not clear and may be due to an immiscibility gap in the $Ti_xZr_{7-x}Ni_{10}$ phase diagram. The lower Ti content in C15 secondary phase in ZN05 and ZN06 causes a reduction in PCT plateau pressure [27] and reduce its catalytic contribution to electrochemical properties.

### 3.2. Hydrogen gas storage properties

Hydrogen gas storage properties were studied by PCT and the resulting absorption and desorption isotherms measured at 30, 60, and 90 °C are shown in Fig. 6. Isotherms from ZN01 are similar to the one-step absorption and two-step desorption reported for annealed $Zr_7Ni_{10}$ [36]. The absorption plateau pressure, isotherm hysteresis, and the slope factor of the non-annealed sample are larger than those of the annealed one, which indicates compositional inhomogeneity and a higher degree of disorder [37]. The $\beta$-to-$\alpha$ transition plateau was not seen due to the low plateau pressure, which was below our pressure measurement limit at these relatively low temperatures ($\leq$90 °C). At 30 °C, even the $\gamma$-to-$\beta$ plateau

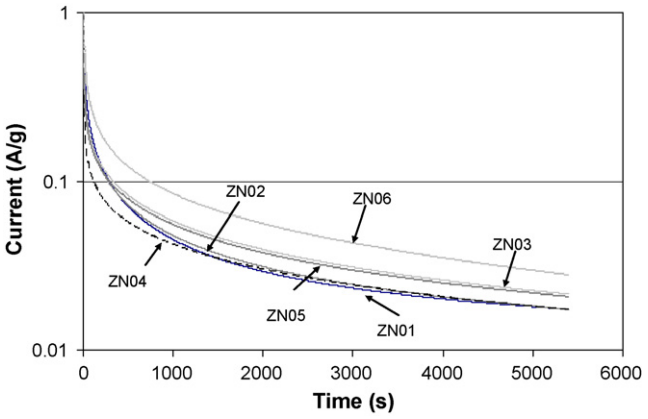


**Fig. 9.** Semilogarithmic curves of anodic current vs. time during potentiostatic discharge of alloys ZN01 to ZN06.

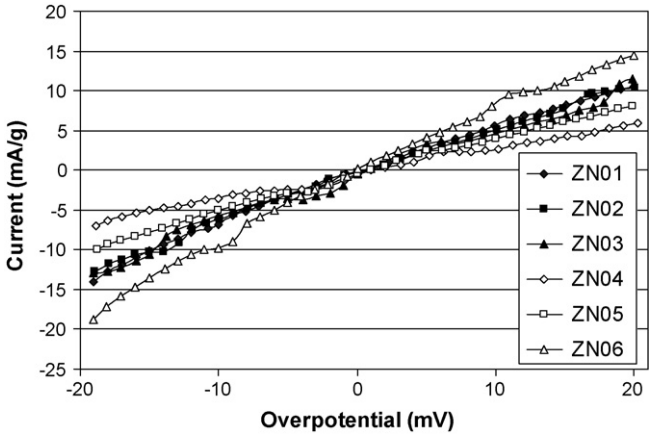


**Fig. 10.** Linear polarization curves of $Ti_xZr_{7-x}Ni_{10}$ alloy electrodes at 50% depth of discharge and 298 K.

was not observed due to the limit of measurement. Entropy and enthalpy of ZN01 $\alpha$-to-$\gamma$ were calculated from 60 to 90 °C absorption isotherms and results are listed in Table 1. The results are close to values reported on annealed $Zr_7Ni_{10}$ ($\Delta H = -49$ kJ/mol and $\Delta S = -132$ J/K mol) [36].

As the titanium substitution level ($x$) in $Ti_xZr_{7-x}Ni_{10}$ was increased, the maximum hydrogen storage capacity generally decreased. This trend is consistent with a smaller lattice constant for higher $x$ value reported in the XRD. As the measurement temperature went up, the absorption and desorption isotherms of all Ti-substituted alloys (ZN02 to ZN06) congregated together, while they diverged from that of the un-substituted ZN01. The sudden increase of plateau pressure with Ti-substitution can be explained by the contribution to a higher electron density from Ti. The grouping of isotherms at 90 °C for all substituting alloys is caused by the similar diffused $\alpha$-state of the hydride below the equilibrium pressure. The absorption isotherms of some substituted alloys (ZN03, 04 and 05) at 30 °C show a two-step isotherm which is different from ZN01. The two-step absorption in these alloys is connected to the extra tetragonal phase in the as-prepared samples. This finding in $Ti_xZr_{7-x}Ni_{10}$ is different from $Hf_xZr_{7-x}Ni_{10}$ study where a two step absorption isotherm was not observed in the entire substitution range ($x = 0$–7) [25]. XRD analyses on these $Hf_xZr_{7-x}Ni_{10}$ samples showed an orthorhombic structure and correlated well to the mono absorption pressure plateau in the entire substitution range. Both the $\alpha$-to-$\beta$ and $\beta$-to-$\gamma$ plateau pressures in 30 °C isotherms go up with increased Ti-substitution. The $\beta$-to-$\gamma$ plateau pressure of ZN06 was above the PCT pressure measuring range therefore it missed one step in the absorption isotherm. The entropy and enthalpy of ZN02, ZN03, and ZN04 were calculated based on the $\alpha$-to-$\beta$ absorption plateau and the results are listed in Table 1. These three heats of formation are very similar and suitable for battery application [38]. No correlation between the heat of formation and the Ti substitution amount can be established, which is different than ZrTiNi Laves phase based alloys [27]. Heat formation grouping of formation may be related to the alloy structure and needs further investigation. The isotherm plateau pressure of ZN05 and ZN06 are too high to be measured and therefore the thermodynamic data of those two alloys cannot be calculated.

### 3.3. Electrochemical study

#### 3.3.1. Discharge capacity measurement

Discharge capacities for alloys ZN01 to ZN06 were measured. Capacities measured at the slowest discharge rate (4 mA/g) for the first 13 cycles for each alloy are plotted in Fig. 7a. All alloys took at least five activation cycles to reach the full capacity. Judging from number of cycles needed to achieve the maximum capacity, activation of alloys with higher Ti contents (ZN04, ZN05, ZN06) was easier than those with lower Ti contents. The same positive contribution of titanium to improved activation was reported by Sawa, et al. on sintered $Zr_7Ni_{10}$ based TiZrNi alloys [22]. The synergetic effect from the secondary phase can be examined by comparing the activation behavior between the unannealed ZN01 sample (this study) and a literature sample annealed at 1000 °C for 30 days [15]. It took about 20 cycles for an unannealed ZN01 to reach a stabilized capacity at 160 mAh/g at a rate of 50 mA/g compared to 50 cycles for an annealed sample with the same chemistry to reach a stabilized capacity of 120 mA/g at a rate of 30 mA/g [15]. The advantage in activation of the unannealed alloy is due to the higher degree of disorder as indicated from both XRD and PCT analyses.

The high rate dischargeability (HRD) (ratio between the capacity measured at fast rate (50 mA/g) and slow rate (4 mA/g)) is plotted in Fig. 7b for the first 13 cycles of each alloy. HRD improves with cycle for every alloy in this study. The HRD of alloys with higher Ti contents (ZN04, ZN05, ZN06) is better than those with lower Ti contents. The discharge capacities at three different rates (after the $10^{th}$ cycle) are plotted against composition in Fig. 8. As $x$ value increases, the capacitiy first decreases and then increases to its maximum and then decreases again. The highest capacity was 201 mAh/g obtained from ZN04 ($Ti_{1.5}Zr_{5.5}Ni_{10}$). It may be related to the smallest amount C15 secondary phase in this alloy.

#### 3.3.2. Diffusion coefficient measurement

Hydrogen diffusion coefficients for various alloys were measured electrochemically using a potentiostatic discharge method. Fig. 9 plots the current response semi-logarithmically vs. time for electrodes which were fully charged then held at a potential +0.6 V vs. open circuit. In the beginning of the curve (time <500 s) the current response is dominated by surface reaction and follows the Butler–Volmer equation. In the later stage of the curve (time > 2000 s) the current response is driven by bulk diffusion of hydrogen and is linear over time following the Eq. (1):

$$\log i = \log\left(\frac{6FD}{da^2}(C_o - C_s)\right) - \frac{\pi^2 D}{2.303\,a^2}t \quad (1)$$

In which $F$ is the Faraday constant, $i$ is the diffusion current density (A/g), $D$ is the hydrogen diffusion coefficient ($cm^2/s$), $d$ is the density of the hydrogen storage alloy, $a$ is the alloy particle radius (cm), $C_O$ is the initial hydrogen concentration in the bulk, $C_S$ is the hydrogen concentration on the surface, and $t$ is the discharge time.

Solving Eq. (1) for $D$ gives the Eq. (2) [40]:

$$D = -\frac{2.303\,a^2}{\pi^2}\frac{\mathrm{d}\log i}{\mathrm{d}t} \quad (2)$$

The diffusion coefficient, $D$, was calculated for the alloys using an average particle radius of $a = 20\,\mu$m and the results are given in Table 1. The calculation for $D$ in Table 1 shows the general trend of an increasing diffusion coefficient from $5.7 \times 10^{-10}$ to $12.1 \times 10^{-10}\,\mathrm{cm}^2/\mathrm{s}$ with increased Ti content. The increased diffusion rate with increased Ti content is confirmed with the HRD measurements also shown in Table 1. The sudden drop of diffusion coefficient in ZN04 is due to the dramatic reduction in the amount of C15 secondary as seen in XRD analysis. Similar reduction in electrochemical kinetic of $ZrCr_{0.7}Ni_{1.3}$ due to the decrease in C15/$Zr_7Ni_{10}$ interface area by annealing was previously reported [39]. According to its higher plateau pressure and higher C15 content, ZN06 should have a larger diffusion coefficient than ZN05 has. However, the diffusion coefficient of ZN06 is smaller than that of ZN05, which is confirmed by the drop in high rate dischargeability listed in Table 1 (84% to 81%). The drop in diffusion coefficient from ZN05 to ZN06 is due to the loss in some storage capacity. As the titanium content increases, the lattice constants become smaller and the site occupancy decreases. The smaller number of available interstitial sites for hydrogen to tunnel through is the cause of the decrease in the diffusion coefficient.

### 3.3.3. Exchange current measurement

The exchange current, a measure of the kinetics in the electrochemical hydrogen reaction at the surface of the electrode, was calculated from the polarization of electrodes. When the overpotential ($\eta$) is changed within a small range ($\eta < RT/\alpha nF$) the Butler–Volmer equation can be simplified to [41]:

$$I = I_0\frac{F}{RT}\eta \quad (3)$$

Where $I$ is the measured current (mA/g), $I_0$ is the exchange current (mA/g), $R$ is the molar gas constant (8.31447 J/mol K), $T$ is the temperature (K), $\alpha$ is the charge-transfer coefficient and $n$ is the number of electrons in the reaction. $RT/F$ is a constant when held at a constant temperature giving a linear relationship between current and overpotential. The exchange current can be measured from the slope in Fig. 10. The exchange currents measured at 50% depth-of-discharge for the alloys are shown in Table 1. From the table one can see initially the exchange current density decreasing with increased titanium content hitting a minimum value at alloy ZN04. After ZN04 the exchange current increases with further increase in titanium. ZN04 and ZN05 are the only two alloys with an undetectable amount of C15 secondary phase and therefore the contribution of C15 phase to the surface kinetics is proven.

## 4. Summary

The microstructure, gas phase hydrogen storage, and electrochemical properties of a series of $Ti_xZr_{7-x}Ni_{10}$ ($x$ between 0 and 2.5) alloys were studied. Alloys prepared by arc melt without further thermal treatment showed a major Laves C15 secondary phase, which is proved to improve both the hydrogen bulk diffusion and surface kinetics. Ti substitution in the alloy produces, in general, better kinetics, improved activation and high rate dischargeability making it a promising candidate for further work in substitution to improve the capacity.

## References

[1] H.T. Takeshita, S. Kondo, H. Miyamura, N. Takeichi, N. Kuriyama, T. Oishi, J. Alloys Compd. 376 (2004) 268.
[2] J.Y. Yu, Y.Q. Lei, C.P. Chen, J. Wu, Q.D. Wang, J. Alloys Compd. 231 (1995) 578.
[3] D. Sun, M. Latroche, A. Percheron-Guégan, J. Alloys Compd. 248 (1997) 215.
[4] M. Bououdina, H. Enoki, E. Akiba, J. Alloys Compd. 281 (1998) 290.
[5] Q.A. Zhang, Y.Q. Lei, X.G. Yang, K. Ren, Q.D. Wang, J. Alloys Compd. 292 (1999) 236.
[6] L. Chen, F. Wu, M. Tong, D.M. Chen, R.B. Long, Z.Q. Shang, H. Liu, W.S. Sun, K. Yang, L.B. Wang, Y.Y. Li, J. Alloys Compd. 293–295 (1999) 508.
[7] K.Y. Shu, X.G. Yang, S.K. Zhang, G.L. Lü, Y.Q. Lei, Q.D. Wang, J. Alloys Compd. 306 (2000) 122.
[8] Y.L. Du, X.G. Yang, Q.A. Zhang, Y.Q. Lei, M.S. Zhang, Int. J. Hydrogen Energy 26 (2001) 333.
[9] Y.H. Zhang, P. Li, X.L. Wang, Y.F. Lin, X.H. Qu, J. Alloys Compd. 364 (2004) 289.
[10] A. Visintin, H.A. Peretti, F. Ruiz, H.L. Corso, W.E. Triaca, J. Alloys Compd. 428 (2007) 244.
[11] K. Young, T. Ouchi, M.A. Fetcenko, J. Alloy Compd. (2008), doi:10.1016/j.jallcom.2008.09.146.
[12] J.M. Joubert, M. Latroche, A. Percheron-Guégan, J. Alloys Compd. 231 (1995) 494.
[13] J.M. Joubert, M. Latroche, A. Percheron-Guégan, J. Bouet, J. Alloys Compd. 240 (1996) 219.
[14] W.K. Zhang, C.A. Ma, X.G. Yang, Y.Q. Lei, Q.D. Wang, Trans. Nonferrous Met. China 19 (1999) 505.
[15] F.C. Ruiz, E.B. Castro, S.G. Real, H.A. Peretti, A. Visintin, W.E. Triaca, Int. J. Hydrogen Energy 33 (2008) 3576.
[16] J.M. Joubert, D. Sun, M. Latroche, A. Percheron-Guégan, J. Alloys Compd. 253–254 (1997) 564.
[17] J.C. Sun, S. Li, S.J. Ji, J. Alloys Compd. 404–406 (2005) 687.
[18] F.H.M. Spit, J.W. Drijver, W.C. Turkenburg, S. Radelaar, J. Phys. 41 (1980) C8–890.
[19] F.H.M. Spit, J.W. Drijver, S. Radelaar, Scr. Metall. 14 (1980) 1071.
[20] H. Sawa, K. Ohzeki, M. Ohta, H. Nakano, S. Wakao, Z. Phys. Chem. Neue Folge 164 (1989) 1527.
[21] M.E. Badding, M.T. McCormack, D.W. Murphy, B. Vyas, US Patent 5,560,752 (1996).
[22] H. Sawa, M. Ohta, H. Nakano, S. Wakao, Z. Phys. Chem. Neue Folge 164 (1989) 1527.
[23] J.L. Glimois, P. Forey, J. Feron, C. Becle, J. Less-Comm. Met. 78 (1981) 45.
[24] C.H. Liu, W.R. Chiangm, K.C. Hsieh, Y.A. Chang, Intermetallics 14 (2006) 1011.
[25] H.T. Takeshita, N. Fujiwara, N. Takeichi, H. Senoh, T. Oishi, J. Alloys Compd. 404–406 (2005) 609.
[26] I. Noriyasu, Japan Patent Hei6-57358 (1994).
[27] K. Young, M.A. Fetcenko, F. Li, T. Ouchi, J. Alloy Compd. 464 (2008) 238.
[28] S.R. Ovshinsky, M.A. Fetcenko, J. Ross, Science 260 (1993) 176.
[29] K. Young, T. Ouchi, Y. Liu, B. Reichman, W. Mays, M.A. Fetcenko, unpublished.
[30] H.T. Takeshita, N. Fujiwara, T. Oishi, D. Noréus, N. Takeichi, N. Kuriyama, J. Alloys Compd. 360 (2003) 250.
[31] M.E. Kirkpatrick, J.F. Smith, W.L. Larsen, Acta Crystallogr. 15 (1962) 894.
[32] J.M. Joubert, R. Černý, K. Yvon, M. Latroche, A. Percheron-Guégan, Acta Crystallogr. C53 (1997) 1536.
[33] Nihon Kinzoku Gakkai, Hi Kagaku Ryouronteki Kinzoku Kagobutu, Maruzen, Tokyo, 1975, p. 296.
[34] R.L. Johnson, R. Hoffmann, Z. Anorg. Allg. Chem. 616 (1992) 105.
[35] Q.A. Zhang, Y.Q. Lei, J. Alloys Compd. 368 (2004) 362.
[36] H.T. Takeshita, T. Kiyobayashi, H. Tanaka, N. Kuriyama, M. Haruta, J. Alloys Compd. 311 (2000) L1.
[37] K. Young, M.A. Fetcenko, T. Ouchi, F. Li, J. Koch, J. Alloy Compd. (2008), doi:10.1016/j.jallcom.2008.01.134.
[38] Y. Osumi, Suiso-kyuzo-goukin no Syurui to Sono, new ed., Agune Technology Center, Tokyo, Japan, 1999, p. 477.
[39] M. Bououdina, C. Lenain, L. Aymard, J.L. Soubeyroux, D. Fruchart, J. Alloy Compd. 327 (2001) 178.
[40] H. Pan, N. Chen, M. Gao, R. Li, Y. Lei, Q. Wang, J. Alloy Compd. 397 (2005) 306.
[41] P.H.L. Notten, P. Hokkeling, J. Electrochem. Soc. 138 (1991) 1877.